Journal of Materials Chemistry A

Accepted Manuscript

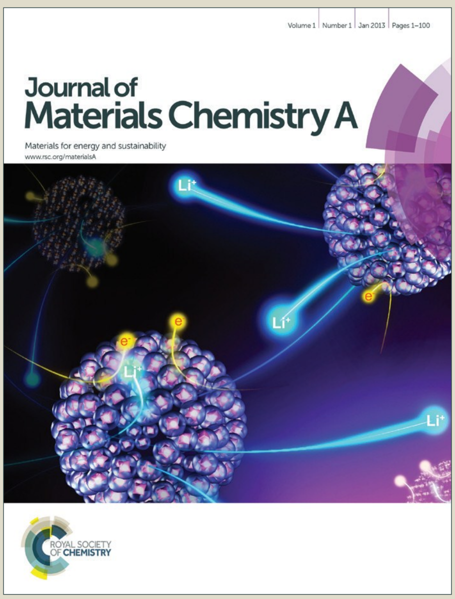

ROYAL SOCIETY OF CHEMISTRY

www.rsc.org/materialsA

Journal Name

ARTICLE

Keplerate-type Polyoxometalate/Semiconductor Composite Electrode with Light-enhanced Conductivity towards High Efficient Photoelectronic Devices

Received 00th January 20xx,
Accepted 00th January 20xx

DOI: 10.1039/x0xx00000x

www.rsc.org/

Shasha Xu,‡[a] Yanhua Wang,‡[a] Yue Zhao,[c] Weilin Chen,*[a] Jiabo Wang, [a] Lifei He,[a] Zhongmin Su,[a] Enbo Wang*[a] and Zhenhui Kang*[b]

Metal oxide semiconductor (MOS) photoelectrodes hold great promise for new energy and environment applications, from water splitting to photoelectronic devices. Here, we show an effecient polyoxometalate asisstance strategy for the design and fabrication of MOS composite photoelectrode with light enhanced conductivity. Four type MOS based photoelectrodes were fabricated by a simple wet chemistry method through bounding TiO_2, SnO, WO_3, ZnO with keplerate-type polyoxometalate $(NH_4)_{42}[Mo^{VI}_{72}Mo^{V}_{60}O_{372}(CH_3COO)_{30}(H_2O)_{72}]$ ({Mo_{132}}), respectively. In these photoelectrodes, {Mo_{132}} may act as photo-induced electron acceptor/donor to accelerate electron transfer and then improve their conductivity efficently. We further demenstrated that the 5%{Mo_{132}}/TiO_2 modified photoanode, in dye-sensitized solar cells (DSSCs), exhibits the power conversion efficiency (PCE) of 7.94% (31% improvement compared with the TiO_2-based cell (6.06%)).

Introduction

The metal oxide semiconductor (MOS; i.e., TiO_2, ZnO and WO_3) electrodes, with the characteristic of photoelectric response, hold great promise for the new energy and photoelectronic devices application, such as, water photoelectrocatalysis, light emission, dye- and quantum-dots-sensitized solar cells, etc.[1-10] Generally, for photoelectronic devices application, a good conductivity (and/or photo-induced conductivity) and visible light induced photoelectric response of these MOS photoelectrodes will enhance their performance and usable capacity greatly.[11-12] Much progress has been achieved in the development of MOS based photoelectrodes for high performance photoelectronic devices. For examples, using the electron acceptor to transfer the electrons quickly from the conduction band (CB) of MOS to external circuit, reducing the electron recombination and enhancing the overall power conversion efficiency (PCE).[13] Meanwhile, the interfacial electron transfer in nanosized materials also varies with the size and the morphology of the materials; and then, various nanostructured semiconductors have been designed with short charge diffusion length, high crystallinity and more charge separation sites, but less defects have been fabricated.[14-17] Moreover, the formation of a semiconductor hetero-junction is also extensively applied to improve the charge separation and transformation.[18,19] However, many MOS photoelectrodes (i.e., TiO_2 and WO_3) still suffer from the poor conductivity and low PCE, which are greatly limited by the low electron diffusion coefficient and the high interfacial electron-hole recombination.[20]

Polyoxometalate (POM), as a nanosized multi-functional species, should be an ideal candidate for photovoltaic application. Our previous studies have shown that POM, in MOS based solar photovoltaic system, can act as the electron acceptor or the electron donor to raise the PCE.[21-27] Motivated by the strong photoelectric activities of POM, we further expect that combining a suitable POM species with MOS as a way to construct MOS composite photoelectrode with light enhanced conductivity for high performance photoelectronic devices. Achim Müller, the famous scientist, has made outstanding contributions in the high-nuclear clusters field.[28] In that POM family, keplerate-type species, $(NH_4)_{42}[Mo^{VI}_{72}Mo^{V}_{60}O_{372}(CH_3COO)_{30}(H_2O)_{72}]$ ({Mo_{132}}) clusters capture our attentions as the photo-induced electron acceptor or electron donor to enhance the conductivity of MOS electrodes owing to its strong absorption in visible light, high stability and unique photoelectric properties. Here, we show a general and efficient POM assistance strategy for the design and fabrication of MOS composite photoelectrodes with light enhanced conductivity. Four kinds of MOS film electrodes

[a]Key Laboratory of Polyoxometalate Science of Ministry of Education, Department of Chemistry, Northeast Normal University, Changchun 130024 (P. R. China). E-mail: chenwl@nenu.edu.cn; *wangeb889@nenu.edu.cn
[b]Institute of Functional Nano & Soft Materials (FUNSOM) and Collaborative Innovation Center of Suzhou Nano Science and Technology, Soochow University, Suzhou, 215123, China. E-mail: zhkang@suda.edu.cn
[c]Department of Vascular Surgery, The China-Japan Union Hospital of Jilin University, Changchun, 130033, China.
†Electronic Supplementary Information (ESI) available: the structure of {Mo_{132}}, TG, XPS spectrum of {Mo_{132}}/TiO_2, XRD patterns of SnO_2, WO_3 and ZnO, SEM, photocurrent response and EIS experiments of ZnO and SnO_2, photovoltaic measurements using different of *n*%{Mo_{132}}/TiO_2, See DOI: 10.1039/x0xx00000x
‡These two authors are equally contributed to this paper.

were fabricated by combining {Mo_{132}} with MOS, denoted as {Mo_{132}}/MOS (TiO_2, ZnO, WO_3, and SnO_2). In these composite photoelectrodes, {Mo_{132}} clusters act as photo-induced electron acceptor/donor to accelerate electron transfer, improve the electron lifetime and retard the recombination, and then lead to the photo-enhanced conductivity. Further, {Mo_{132}}/TiO_2 composite photoelectrodes were introduced into the DSSCs as the photoanode. The 5%{Mo_{132}}/TiO_2 photoanode exhibits the PCE of 7.94%, increased by 31% compared with the TiO_2-based cell (PCE, 6.06%).

Results and discussion

Properties of {Mo_{132}}

{Mo_{132}}, a nanoball reported by Achim Müller in 1998, has a fascinating and special structure with more than 500 atoms and the highest Euclidean symmetry.[28-30] The anion of {Mo_{132}} is a spherical icosahedral cluster (a nanoball), which is composed of 12 {Mo_{11}} fragments with a central bipyramidal pentagonal {MoO_7} unit to form a cage structure (see Fig. S1†). About {Mo_{132}}, most previous reports mainly focused on its structure and basic catalytic properties.[30] Here, some basic electrochemical and photoelectric properties of {Mo_{132}} were further investigated in our experiments. Scanning electron microscopy (SEM) image (Fig. 1a) and transmission electron microscopy (TEM) profile (upper inset in Fig. 1a) of the prepared {Mo_{132}} display that {Mo_{132}} nanoballs can be self-assembled to be the aggregates with the size ranging between 1 and 2.5 μm. Energy dispersive spectrometry (EDS) further demonstrates the existence of Mo, C and O in the {Mo_{132}} aggregates (down inset in Fig. 1a). The UV-vis absorption of {Mo_{132}} exhibits a broad optical absorption band nearly covering the whole of UV and visible regions (Fig. 1b), which is beneficial for solar energy harvesting. The UV light absorption is attributed to the charge transfer from oxygen to metal and the visible absorption is due to Mo^V *d-d* transitions and Mo^V-Mo^{VI} intervalence charge transfer transition in the {Mo_{132}} framework.[31] The electron energy levels of {Mo_{132}} were also studied by the cyclic voltammetry (CV), solid diffuse reflection method, as well as the ultraviolet photoemission spectroscopy (UPS) techniques. The lowest unoccupied molecular orbital (LUMO) energy level of POM is formally a combination of *d* orbits centering on the metal atoms, which could be estimated from the first reduction applied potential of the CV.[32] It can be confirmed from Fig. 1c that the LUMO level of {Mo_{132}} corresponds to -0.52 V *vs* Ag/AgCl, which is equal to -0.33 V *vs* NHE and -4.17 eV *vs* vacuum. The band gap energy (E_g) of {Mo_{132}} was acquired from the diffuse reflectance UV-vis spectrum. Fig. 1d reveals the plot of *K-M* function *F* against energy *E* of {Mo_{132}}. The E_g of {Mo_{132}} was estimated to be 1.61 eV by measuring the *x*-axis intercept of an extrapolated line from the linear regime of the curve.[33] The UPS measurement of {Mo_{132}} was carried out to gain more insight into the energy levels. As shown in Fig. 1e, the work function (W_F) of the {Mo_{132}} is calculated to be about 2.84 eV by subtracting the width of the secondary electron cutoff (18.38 eV) from the excitation energy (21.22 eV). The ionization energy (I_E, the onset of the band of occupied orbital) of {Mo_{132}} is about 2.96 eV, and then the highest occupied molecular orbital (HOMO) of {Mo_{132}} with respect to vacuum level can be caculated from -(W_F+I_E), which is -5.80 eV.[4,34,35] On the basis of the UPS and UV-vis spectrum results, the LUMO of {Mo_{132}} can be got to be -4.19 eV, which is well agreement with the result gained from the CV test (-4.17 eV *vs* vacuum). Fig. 1f shows the energy levels of {Mo_{132}}, the reported theoretical calculation data of {Mo_{132}},[36] and the band structure of common MOSs. It suggests that the energy levels (HOMO/LUMO) of {Mo_{132}} are in a mediate position of band structure (VB/CB) of common MOSs, which satisfy the necessary condition for {Mo_{132}} improving the conductivity of {Mo_{132}}/MOS composite electrodes by the electron acceptation or donation. In addition, the TG curve and IR spectra of {Mo_{132}} (Fig. S2†) demonstrate that the skeleton structures of {Mo_{132}} remain stable below 210 °C, indicating a good stability of {Mo_{132}}/MOS composite during the fabrication.

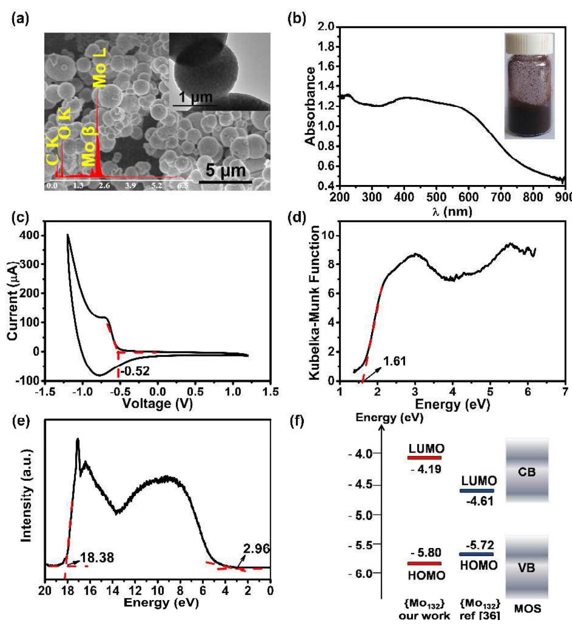

Fig. 1 (a) The SEM image of {Mo_{132}} clusters. Insert: TEM image and the EDS diagram of {Mo_{132}}. (b) The UV-vis spectrum of {Mo_{132}}. Insert: the solid sample photo of {Mo_{132}}. (c) The CV curve of {Mo_{132}} in Na_2SO_4/H_2SO_4 solution at pH = 4.00. The red lines are the tangents of the curve. The intersection value is the LUMO of {Mo_{132}} *vs* Ag/AgCl. (d) The plot of *F* against energy *E* for {Mo_{132}}. The red line is the tangent of the curve and the intersection value is the band gap. (e) UPS photoemission spectrum of {Mo_{132}}. The red lines are the tangents of the curve. The intersections of the tangents give the edges of the UPS spectra from which the ionization energy (I_E) and the work function (W_F) are determined. (f) The energy levels of {Mo_{132}} (red line: our work; blue line: the theoretical calculation value based on ref. 36); CB and VB represent a range.

$\{Mo_{132}\}/TiO_2$ Composite Photoelectrodes

In the first set of experiments, we studied the photo-electronic chemical properties of $\{Mo_{132}\}$/MOS composite photoelectrodes. Briefly, the TiO_2 paste prepared by mixing $\{Mo_{132}\}$ and the calcined TiO_2 with the mass percentage of 5% (5% $\{Mo_{132}\}$; 95% TiO_2) was fabricated to be the composite photoelectrode (5%$\{Mo_{132}\}/TiO_2$ photoelectrode), and the pure TiO_2 for comparison.[37] The SEM image (Fig. 2a) of 5%$\{Mo_{132}\}/TiO_2$ photoelectrode indicates that it consists of spherical and granular particles with size in range from 20 to 100 nm. Furthermore, the EDS mapping (Fig. 2b) demonstrates the existence of Ti, Mo, C and O, which confirms that $\{Mo_{132}\}$ and TiO_2 are uniformly distributed in the composite photoelectrodes. X-ray diffraction (XRD) was carried out to monitor the TiO_2 phase changes in the 5%$\{Mo_{132}\}/TiO_2$ composite photoelectrodes. The characteristic peaks of TiO_2 can be discovered from the XRD patterns of calcined TiO_2 and 5%$\{Mo_{132}\}/TiO_2$ (Fig. 2c), which are in agreement with those of anatase TiO_2 (JCPDS, 21-1272), indicating that the crystal shape of TiO_2 was not changed after the modification with $\{Mo_{132}\}$. The diffraction peaks for $\{Mo_{132}\}$ are not effectively detected from the XRD patterns of 5%$\{Mo_{132}\}/TiO_2$ due to the lower content of $\{Mo_{132}\}$ or its amorphous state.[38] The X-ray photoelectron spectrum (XPS) of TiO_2, $\{Mo_{132}\}$ and 5%$\{Mo_{132}\}/TiO_2$ composite was employed to further analyze the surface composition and chemical environment of Ti and Mo atoms. As shown in Fig. S3† and Fig. 2d, the XPS spectra of 5%$\{Mo_{132}\}/TiO_2$ clearly reveals the presence of O (1s), Ti (2p), C(1s) and Mo (3d). For pure TiO_2, the energy regions of Ti $2p_{3/2}$ and Ti $2p_{1/2}$ are located at 457.8 and 463.4 eV. While, both of Ti $2p_{3/2}$ and Ti $2p_{1/2}$ energy regions shift towards the lower binding energy and locate at 457.4 and 463.2 eV for 5%$\{Mo_{132}\}/TiO_2$ composite.[39,40] Fig. 2e clearly illustrates that the characteristic Mo3d doublet is composed of the $3d_{5/2}$ and $3d_{3/2}$ levels. In the lower group curves of the XPS of $\{Mo_{132}\}$, the peaks located at 231.9 eV and 235.1 eV are assigned as Mo^{VI}, while the peaks at 234.1 eV and 231.1 eV are attributed to Mo^{V}.[41,42] Furthermore, the XPS peaks of Mo in 5%$\{Mo_{132}\}/TiO_2$ also shift towards a lower binding energy compared with the pure $\{Mo_{132}\}$. All these XPS results indicate that the $\{Mo_{132}\}$ has indeed been combined with TiO_2 in the 5%$\{Mo_{132}\}/TiO_2$ composite, but not the physical mixture of $\{Mo_{132}\}$ and TiO_2. Fig. 2f represents the powder UV-vis absorption of TiO_2, 5%$\{Mo_{132}\}/TiO_2$ and pure $\{Mo_{132}\}$. Pure TiO_2 only absorbs UV light (λ<387 nm) without any absorption in the visible and infrared regions. While the strong UV and visible absorption could be observed for 5%$\{Mo_{132}\}/TiO_2$ composite.

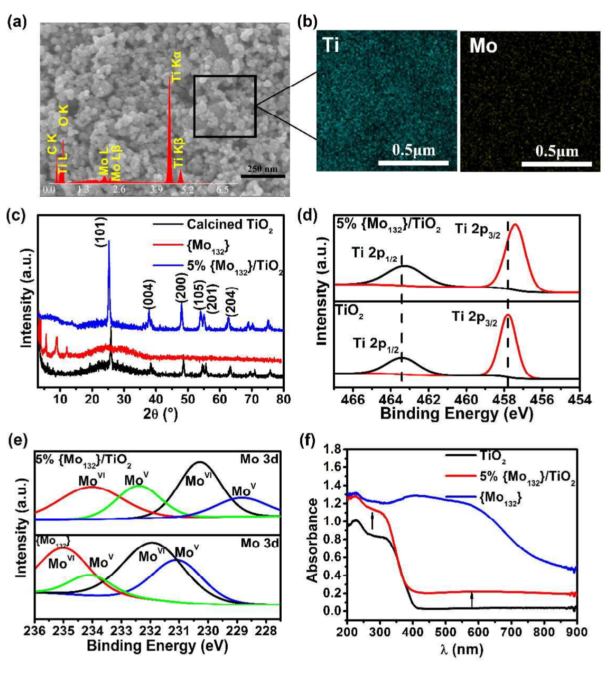

Fig. 2 (a) The SEM image 5%$\{Mo_{132}\}/TiO_2$ film electrode. Inset: the EDS diagram. (b) Elemental mappings of Ti and Mo. (c) XRD patterns of $\{Mo_{132}\}$ (red line), calcined TiO_2 (black line) and 5%$\{Mo_{132}\}/TiO_2$ (blue line). (d) and (e) High resolution XPS spectra of Ti 2p and Mo 3d after Gaussian curve fitting. (f) UV-vis spectra of TiO_2 (black line) and 5%$\{Mo_{132}\}/TiO_2$ (red line) and $\{Mo_{132}\}$ (blue line).

The photocurrent response and electrochemical impedance spectroscopy (EIS) are the valuable measurements to study the conductivity of the surface-modified electrodes, in particular regarding the electron-transfer characteristics.[43] The photocurrent transient experiments have been carried out under the simulated solar illumination for the 5%$\{Mo_{132}\}/TiO_2$ and the TiO_2 film electrodes to investigate the conductivity of the electrodes with the introduction of $\{Mo_{132}\}$. Fig. 3a presents the photocurrent changes of the film electrodes when the irradiation is switched on and off. The photocurrent density of pure TiO_2 is approximately 0.015 $mA{\cdot}cm^{-2}$, and this weak photocurrent response may be due to its fast electron-hole recombination and weak absorption in the visible area. Strikingly, the photocurrent response intensity of the 5%$\{Mo_{132}\}/TiO_2$ (about 0.059 $mA{\cdot}cm^{-2}$) is four times higher than that of pure TiO_2. Furthermore, the photocurrent at different irradiance is shown in Fig. 3b, the 5%$\{Mo_{132}\}/TiO_2$ film electrode shows a higher photocurrent response for different light intensities compared to the pure TiO_2, which also testifies that the conductivity of TiO_2 is virtually enhanced by the incorporation of $\{Mo_{132}\}$. The reason may be that $\{Mo_{132}\}$ can compensate the weak absorption of TiO_2 in the visible region.

The investigations of EIS presented in the forms of a typical Nyquist plots are to understand the difference in the electronic properties of 5%$\{Mo_{132}\}/TiO_2$ and TiO_2 film electrodes (Fig. 3c). The semicircle diameter at high frequency corresponds to the charge-transfer resistance (R_{ct}), and a straight line at low frequency attributes to diffusion process, which represents the so-called Warburg impedance.[44] The analog circuit diagram of equivalent circuit used to fit the impedance measurement has been illustrated in Fig. S4†. The diameter for arc radius of the 5%$\{Mo_{132}\}/TiO_2$ electrode is smaller than the TiO_2 electrode, which indicates that the conductivity is enhanced by the modification of TiO_2 with

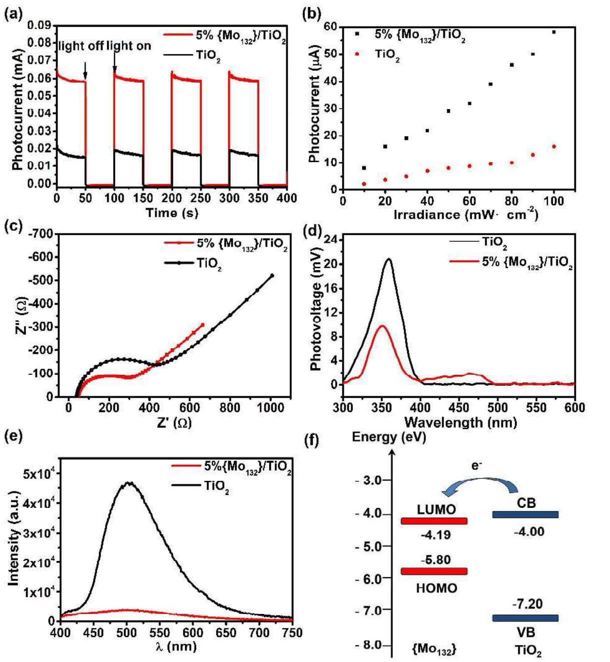

Fig. 3 (a) Photocurrent responses with on-off light illumination under the simulated AM 1.5 illumination at 100 mW•cm^{-2}. (b) Photocurrent at different irradiance. (c) Nyquist plots of TiO_2 (black line) and 5%{Mo_{132}}/TiO_2 (red line). (d) SPS of TiO_2 (black line) and 5%{Mo_{132}}/TiO_2 (red line). (e) The emission spectra of TiO_2 (black line) and 5%{Mo_{132}}/TiO_2 (red line). (f) Energy levels of TiO_2 (blue line) and {Mo_{132}} (red line). The arrow represents the direction of electron transfer.

{Mo_{132}}. {Mo_{132}} may enhance the injection and transport of electrons, and then retard the electrons recombination in the TiO_2 film electrode. The surface photovoltage spectrum (SPS) and the photoluminescence (PL) were also further utilized to survey the charge transfer process at the interface of TiO_2 and {Mo_{132}} in the electrode. The SPS of pure TiO_2 suggests a peak around 360 nm (Fig. 3d), which may be ascribed to the charge separation upon only UV light excitation. The 5%{Mo_{132}}/TiO_2 composite reveals higher photovoltage in the visible region than pure TiO_2 (Fig. 3d), which demonstrates that the modification of {Mo_{132}} could broaden the optical response range of TiO_2. While the SPS response of 5%{Mo_{132}}/TiO_2 (9.72 mV) displays lower photovoltage in the UV region than pure TiO_2 (20.82 mV), which may be attributed to the photogenerated charge transfer between {Mo_{132}} and TiO_2 particles. The electrons accepted by the {Mo_{132}} will recombine with the holes of TiO_2, leading to the lower photovoltage and enhancing the conductivity of the TiO_2.[45] In addition, the change of PL intensities can reveal the photogenerated charge-carrier recombination rate in semiconductors.[27]The PL of pure TiO_2 appears a fluorescence emission band at 500 nm upon the excitation at 390 nm (**Fig. 3**e), which is efficiently quenched (upon the same excitation wavelength) with the introduction of {Mo_{132}} to TiO_2 demonstrating that the photo induced electrons may transfer from TiO_2 to {Mo_{132}} clusters. It can be concluded that the charge recombination is suppressed by the incorporated {Mo_{132}}. The LUMO of {Mo_{132}} is lower than the CB of TiO_2, so {Mo_{132}} can be used as the electron acceptor to accept the electrons from TiO_2, which is a favorable exothermic process (Fig. 3f). The photoelectrons in the excited state can be extracted and transferred to {Mo_{132}}. So {Mo_{132}} may increase the mobility of electrons in the TiO_2 and enhance the conductivity of the electrode.

{Mo_{132}}/MOS (ZnO, WO_3, SnO_2) Photoelectrodes

In {Mo_{132}}/TiO_2 system, we show that {Mo_{132}} acts as the photo-induced electron acceptor to accelerate electron transfer and then improve their conductivity efficiently. Here the question is whether {Mo_{132}} is a general functional species for the high performance {Mo_{132}}/MOS composite photoelectrodes or not. Similar to TiO_2, ZnO is also a wide band gap (about 3.20 eV) MOS. Similar experiments of {Mo_{132}} modified ZnO film electrodes (Fig. S5† and S6†) with a weight ratio of 5% were also studied under simulated solar illumination. In Fig. S6a† and S6b†, the similar morphology of the ZnO film and 5%{Mo_{132}}/ZnO suggests that the {Mo_{132}} did not affect the morphology of ZnO. The photocurrent response intensity of the 5%{Mo_{132}}/ZnO changes from 0.03 mA·cm^{-2} to 0.08 mA·cm^{-2} (Fig. S6c†). Meanwhile, in Fig. S6d†, the investigation of EIS also proves that {Mo_{132}} may act as the electron acceptor to inhibit the recombination of electron-hole, thus improving the conductivity of the 5%{Mo_{132}}/ZnO film electrode. WO_3 is a MOS material (band gap about 2.70 eV) with the CB edge (−5.24 eV vs vacuum) lower than the LUMO of {Mo_{132}}.[46] The XRD patterns of WO_3 powder (Fig. S7†) indicate that it is the monoclinic phase.[9] In the following experiments, the {Mo_{132}}/WO_3 composite photoelectrode was fabricated by combing {Mo_{132}} and WO_3 nanocrystals with a weight ratio of 5%. The SEM of WO_3 and 5%{Mo_{132}}/WO_3 film electrodes

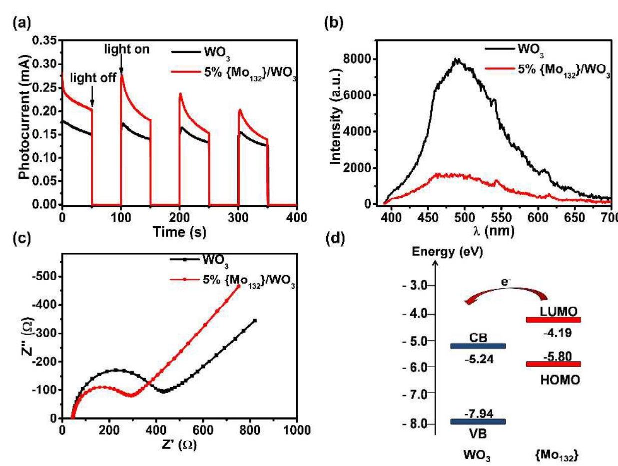

Fig. 4 (a) Photocurrent responses of 5%{Mo_{132}}/WO_3 (red line) and WO_3 (black line). (b) Nyquist plots of 5%{Mo_{132}}/WO_3 (red line) and WO_3 (black line). (c) The emission spectra of 5%{Mo_{132}}/WO_3 (red line) and WO_3 (black line). (d) Energy levels of WO_3 and {Mo_{132}}.

illustrate the morphology of film surface. As shown in Fig. S8a †, the fairly uniform-sized WO_3 nanocrystals are distributed well on the surface. Also, the similar morphology of the 5%{Mo_{132}}/WO_3 film is shown in Fig. S8b†, suggesting that the {Mo_{132}} did not influence the morphology of WO_3. The photocurrent response and EIS experiments of 5%{Mo_{132}}/WO_3 and pure WO_3 film electrodes have been carried out to study the conductivity of the {Mo_{132}}-modified WO_3 film electrodes. It can be observed that the photocurrent density (approximately 0.16 mA·cm^{-2}) of the 5%{Mo_{132}}/WO_3 film electrode increases by about 0.02 mA·cm^{-2} than that of pure WO_3 (0.14 mA·cm^{-2}) (Fig. 4a). In addition, the EIS investigations (Fig. 4b) indicate that the semicircle diameter at high frequency of the 5%{Mo_{132}}/WO_3 film electrode is smaller than that of the WO_3 electrode, which reveals that the charge-transfer resistance on the electrode surface is decreased with the introduction of {Mo_{132}}. The PL experiment was also carried out to understand the efficiency of charge trapping and transfer in the semiconductor. The PL signal intensity at 480 nm for the 5%{Mo_{132}}/WO_3 is much lower than pure WO_3 (Fig. 4c). It also implies that the composite of {Mo_{132}}/WO_3 has a lower recombination rate of electrons and holes, which is mainly attributed to the excited electron transfer from {Mo_{132}} to WO_3. The LUMO potential of {Mo_{132}} is higher than the CB edge of WO_3 (−5.24 eV vs vacuum), so the excited electrons on {Mo_{132}} can be directly injected into the CB of WO_3 under the simulated solar irradiation, and the electrons subsequently transfer to the FTO substrate (Fig. 4d). These results demonstrate that {Mo_{132}} has the extensive applicability to be used as the electron donor. Similarly, the CB of the SnO_2 (−4.50 eV vs vacuum) is also lower than the LUMO of {Mo_{132}}. The photocurrent response and EIS experiments of 5%{Mo_{132}}/SnO_2 and pure SnO_2 film electrodes have been also carried out. The XRD patterns of SnO_2 in Fig. S9† correspond well to the tetragonal SnO_2 (JCPDS, 41-1445).[47] The SEM image of SnO_2 shows the flower structure (Fig. S10a†). Additionally, the SEM image of 5%{Mo_{132}}/SnO_2 reveals that the morphology is not changed after the modification of {Mo_{132}} (Fig. S10b†). In the Fig. S10c†, the photocurrent response 5%{Mo_{132}}/SnO_2 film electrode is increased by about 0.01 mA·cm^{-2} than that of pure SnO_2. The results of the EIS (Fig.S10d†) can also manifest that the {Mo_{132}} has the universality for other MOS film electrodes both as the electron acceptor and donor. As discussed above, {Mo_{132}} can not only be used as the electron acceptor, but also can be used as the electron donor to modulate the conductivity of electrodes under light. Here we further summarize the function and propose mechanism of {Mo_{132}} in {Mo_{132}}/MOS (Fig. 5). Simply, we divide the common MOS into two parts: MOS (I), the CB edge is higher than the LUMO of {Mo_{132}}; MOS(II), the CB edge is lower than the LUMO of {Mo_{132}}. For {Mo_{132}}/MOS(I) system, as shown in Fig. 5a, the electrons in MOS(I) CB edge could be extracted and transferred to {Mo_{132}}, by which {Mo_{132}} can increase the mobility of electrons in the MOS(I) and enhance the conductivity of the MOS based photoelectrode. At the same time, in the interfacial region, electron recombination may be overcome by introducing this kind of a powerful electron acceptor {Mo_{132}}. On the other hand, for {Mo_{132}}/MOS(II) system (see Fig. 5b), {Mo_{132}} is used as the electron donor and the photoelectrons can be injected into the CB of MOS(II) efficiently. At last, the photoresponse property and narrow band gap nature of {Mo_{132}} is also helpful for the present light enhanced conductivity of {Mo_{132}}/MOS (I, II) system.

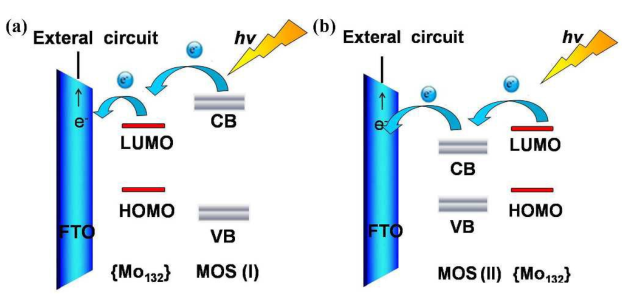

Fig. 5 The scheme of the photo-induced electron transfer mechanism in the MOS electrodes. In 5a, MOS (I) represents a class of metal oxides, whose CB is higher than the LUMO of {Mo_{132}}. {Mo_{132}} clusters act as the electron acceptor. In 5b, MOS (II), the CB edge is lower than the LUMO of {Mo_{132}}. {Mo_{132}} clusters can be used as the electron donor.

{Mo_{132}}/TiO_2 Photoelectrodes Based DSSCs

We further demonstrated the application of 5%{Mo_{132}}/TiO_2 photoanode in dye-sensitized solar cells (DSSCs). Fig. 6a presents the scheme of DSSC based on 5%{Mo_{132}}/TiO_2, which consists of a film of dye (N719)-sensitized {Mo_{132}}/TiO_2 photoelectrode, a Pt counter electrode and the electrolyte containing the redox pairs (I^-/I_3^-). Fig. 6b presents the UV-vis absorption spectra of {Mo_{132}} and N719. Notably, {Mo_{132}} has a good absorption in the visible area at 450 nm, which is expected to make up for the visible absorption of dye N719. The performance of the {Mo_{132}}/TiO_2 DSSCs were investigated under simulated AM 1.5 illumination (at 100 mW·cm^{-2}) and in the dark, respectively. The power conversion efficiency (η) of the {Mo_{132}}/TiO_2 DSSC has the pronounced enhancement compared to the pure TiO_2 DSSC. The {Mo_{132}}/TiO_2 DSSC exhibits a short circuit current density (J_{sc}) of 16.78 mA·cm^{-2}, an open circuit voltage (V_{oc}) of 711 mV and a fill factor (FF) of 0.666, resulting in the η of 7.94% (see Table 1). It indicates an overall PCE improvement up to 31% compared with the TiO_2-based cell (6.06%). The increase of J_{sc} may be due to more efficient electronic injection, smoother transfer and high efficient collection. The improvement of V_{oc} may be ascribed to the reduced charge recombination. Further, 5%{Mo_{132}}/TiO_2 can also decrease the onset of dark current to different extent (Fig. 6c), which may be attributed to the contribution of {Mo_{132}} preventing the electrons flowing back to the electrolyte or dyes from {Mo_{132}}/TiO_2 photoelectrode. Fig. 6d depicts the EIS measurements with 5%{Mo_{132}}/TiO_2

photoanode and the pure TiO_2. The semicircle in high frequency corresponds to R_1, which

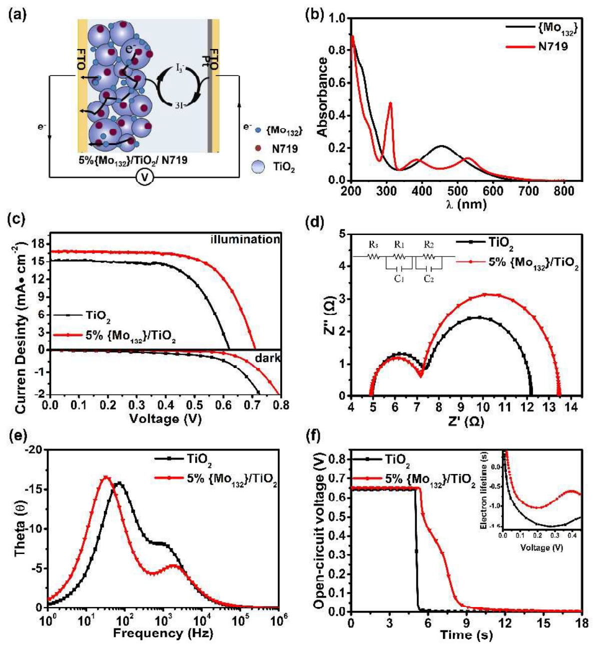

Fig. 6 (a) Schematic diagram of the DSSC. (b) UV-vis absorption spectra of $\{Mo_{132}\}$ (black line) and N719 (red line). (c) *J-V* curves of the DSSCs with $5\%\{Mo_{132}\}/TiO_2$ (red line) and pure TiO_2 (black line) as the photoanodes. Upper group curves: under AM 1.5 simulated solar illumination at 100 $mW{\cdot}cm^{-2}$. The lower group curves: under dark. (d) Nyquist plots of $5\%\{Mo_{132}\}/TiO_2$ (red line) and TiO_2 (black line). Inset: the equivalent circuit. (e) Bode phase plots of $5\%\{Mo_{132}\}/TiO_2$ (red line) and TiO_2 (black line). (f) OCVD curves of $5\%\{Mo_{132}\}/TiO_2$ (red line) and TiO_2 (black line). Inset**:** Electron lifetime of $5\%\{Mo_{132}\}/TiO_2$ (red line) and TiO_2 (black line) calculated from OCVD measurement according to the equation: $\tau = (kT/e)/(dV/dt)$.

represents the charge transfer resistance at the counter electrode/electrolyte interface. The second semicircle (R_2) reflects the electron transport resistance at the photoelectrode/dye/electrolyte interface related to the charge transport/recombination.[48] Here, R_1 is similar since all the cells have the same Pt counter electrode and electrolyte. However, the R_2 of $5\%\{Mo_{132}\}/TiO_2$ photoanode changes from 4.86 Ω (pure TiO_2) to 6.26 Ω, which indicates that $\{Mo_{132}\}$ can retard the charge recombination and result in a smoother and efficient electron transmission in $\{Mo_{132}\}/TiO_2$ photoanode. The bode phase plots are shown in Fig. 6e, the characteristic frequency peak (f_{max}) of $5\%\{Mo_{132}\}/TiO_2$ photoanode at the top of the intermediate frequency arc is 72.20 Hz and the f_{max} of TiO_2 is 31.10 Hz, so the calculated electron lifetime (about 5.12 ms) of the DSSC based $5\%\{Mo_{132}\}/TiO_2$ is longer than TiO_2 (about 2.21 ms) based on the f_{max} values,[49] which are coincident with the dark current measurements, demonstrating an improvement on the retardation of carrier recombination. Meanwhile, the electrons recombining can be further evaluated by the open-circuit voltage decay (OCVD), which monitors the decay of V_{oc} after turning off the

Table 1 Photovoltaic properties of the DSSCs based on different photoanodes. The value of the data in the table was obtained from the average of three parallel DSSCs.

	J_{sc}(mA· cm^{-2})	V_{oc}(V)	FF(%)	η(%)
pure TiO_2	15.28	0.621	0.638	6.06
$5\%\{Mo_{132}\}/TiO_2$	16.78	0.711	0.666	7.94

illumination in a setting time.[50] As shown in **Fig. 6**f, it is evident that the DSSC based on $5\%\{Mo_{132}\}/TiO_2$ photoanode exhibits a slower photovoltage decay rate than that of the pure TiO_2 photoanode, which indicates that the electrons recombining kinetics has been retarded effectively. Further, from the inset of Fig. 6f, we can also conclude that the $5\%\{Mo_{132}\}/TiO_2$ photoanode has the longer electron lifetime than that of pure TiO_2 photoanode, and will lead to the higher charge collection rate of photogenerated electrons and an improvement in the cell efficiency.

In the next study, a series of $\{Mo_{132}\}/TiO_2$ photoanode-based DSSCs were fabricated and their performance are shown in Fig. S11† and S12†. The average performance characteristics obtained from the multiple cells are summarized in Table S1, and the corresponding parameters obtained from the EIS are listed in Table S2. The PCE values of the DSSCs have the pronounced enhancement with the increasing of the content of $\{Mo_{132}\}$ from 1%, 3% to 5%, compared to the performance of pure TiO_2, and the best performance of DSSC is the percentage of $\{Mo_{132}\}$ up to 5%. However, increasing the content of $\{Mo_{132}\}$ up to 7%, the R_2 of $7\%\{Mo_{132}\}/TiO_2$ photoanode reduces to 5.04 Ω (Fig. S12a† and Table S2), the performance of DSSCs would decline and is close to pure TiO_2. It may be attributed to the aggregation of the $\{Mo_{132}\}$ during the paste making process, and then the electrons massively injected into the electrolyte and no longer collected at the anode.[51]

Experimental

Chemical and Reagents

All chemicals were commercially purchased and used without further purification. $\{Mo_{132}\}$ was prepared according to the literature method.[28]

Electrodes Preparation

Firstly, TiO_2 powder was sintered at 450 °C for 30 min. Then the TiO_2 paste was prepared according to the literature by mixing $\{Mo_{132}\}$ and the calcined TiO_2 with a series mass percentage of 0%, 1%, 3%, 5%, and 7% to fabricate the film electrodes.[52] The FTO glass plates were pretreated by immersed into the 40 mM $TiCl_4$ aqueous solution at 70 °C for 30 min, and washed with water and absolute ethanol. The electrodes were prepared by coating one layer of paste on the FTO glass plates by screen-printing followed by drying for 5 min at 120 °C. Four-layered paste was coated on every FTO glass. Then, the film electrodes were calcined at 210 °C for 30 min. Subsequently, the resulting sintered film electrodes were post-treated in 40 mM $TiCl_4$ solution for 30 min at 70 °C and calcined in air at 210 °C for 30 min again. In the meantime, $\{Mo_{132}\}$ modified ZnO, WO_3, SnO_2 in a ratio of 5% electrodes were prepared in the same way.

Solar cells fabrication

The obtained TiO_2 film electrodes were immersed in the 0.2 mM N719 absolute ethanol solution for 24 h. The excess unanchored dyes were rinsed off with absolute ethanol and dried with N_2. Platinum was used as counter electrode. A drop of electrolyte solution composed of 0.1 M LiI, 0.05 M I_2, 0.6 M 1,2-dimethyl-3-propylimidazolium iodide and 0.5 M 4-tert-butylpyridine in 3-methoxypropionitrile was introduced between the electrodes by the injector.

Characterization Methods

IR spectrum was recorded in the range of 400-4000 cm^{-1} region on an Alpha Centaurt FT/IR spectrophotometer with KBr pellet. TG analysis was performed on a PerkinElmer TGA7 instrument at a heating rate of 10 °C min^{-1} from 25 to 600 °C. X-ray powder diffraction data were collected on a Bruker AXS D8 Advance diffractometer using Cu *Kα* radiation (λ = 1.5418 Å) in the 2ϑ range of 3-90^o with a step size of 0.02^o. The diffuse reflectivity spectra were collected on SHIMADZU UV-Vis Spectrophotometer UV-2600 in reflectance mode, which were measured from 200 to 800 nm using barium sulfate ($BaSO_4$) as a standard with 100% reflectance. Ultraviolet photoelectron spectroscopy (UPS) measurement was performed using the ^{1}He (21.22 eV) excitation. The morphology of the samples was characterized with SEM (FESEM; XL30, FEG, FEI Company) and TEM (HitachiH-7650). Energy dispersive X-ray spectroscopy (EDS) was obtained from FEI Quanta 200F microscope. X-ray photoelectron spectroscopy (XPS) measurement was performed with a hemispherical analyzer Leybold EA 11. The fluorescence spectra were recorded on the FL900/FS920 steady-state fluorescence spectrometer.

Photoelectrochemical measurements

Cyclic voltammogram curve was recorded on a CHI601D Electrochemical Workstation (Shanghai CH Instrument Corp., China), using the composite film assembled FTO glass electrodes as the working electrode, a Pt wire as the counter electrode and the reference was a saturated Ag/AgCl electrode. 0.10 M Na_2SO_4/H_2SO_4 solution with pH=4.00 was used as the supporting electrolyte on the premise of stability of $\{Mo_{132}\}$. Electrochemical impedance spectra (EIS) of the electrodes were measured with an impedance analyzer (Compactstat, IVIUM Tech.) at an open-circuit potential under the condition of simulated solar illumination in 0.10 M KCl solution containing equimolar $[Fe(CN)_6]^{3-}/^{4-}$ at an ac frequency from 100 kHz to 0.1 Hz. All electrodes were illuminated from the front side using a 300 W Xe lamp equipped with an AM 1.5 G filter (Model 81094, Newport) to simulate the solar spectrum. The photocurrent transient experiments were carried out at a constant bias of 0 V under simulated solar illumination. The illumination area of working electrode was set constant at 0.25 cm^2. The surface photovoltage spectroscopy (SPS) measurement was carried out on a lab-made instrument, which constitutes a source of monochromatic light, a lock-in amplifier (SR830-DSP) with a light chopper (SR540) and a photovoltaic cell. The photocurrent-voltage (*J-V*) characteristics, electrochemical impedance spectroscopy (EIS) measurements of the DSSCs were conducted on an electrochemical workstation, applying a DC bias at open circuit voltage and an AC voltage with the amplitude of 10 mV in dark conditions. Impedance parameters were determined by fitting of the impedance spectra using Z-view software. Open circuit voltage decay (OCVD) of the DSSCs was measured under AM 1.5 simulated solar illumination at 100 mW·cm^{-2}.

Conclusions

We report a general and efficient polyoxometalate assistance strategy for the design and fabrication of POM/MOS composite photoelectrodes with light-enhanced conductivity. Four $\{Mo_{132}\}$/MOS composite photoelectrodes ($\{Mo_{132}\}/TiO_2$, ZnO, WO_3, SnO_2) were fabricated and investigated to evaluate the light-enhanced conductivity of these composite photoelectrodes. In $\{Mo_{132}\}$/MOS composite photoelectrodes, $\{Mo_{132}\}$ acts as photo-induced electron acceptor/donor to accelerate the electron transfer and then improve their conductivity efficiently. Also, the photoresponse property and narrow band gap nature of $\{Mo_{132}\}$ is also helpful for this light-enhanced conductivity process. We further demonstrated that the 5%$\{Mo_{132}\}/TiO_2$ photoelectrode can be applied in DSSCs as the photoanode. In this system, $\{Mo_{132}\}$ has a good absorption in the visible area at 450 nm, which makes up for the visible absorption of N719. The 5%$\{Mo_{132}\}/TiO_2$ modified photoanode exhibits the largest electron lifetime (5.12 ms), longer than that of pure TiO_2 (2.21 ms) and a high efficiency up to 7.94%, enhanced by 31% compared with that of pure TiO_2 (6.06%). This work may also provide a new way for getting high performance photoelectrodes in many applications, including solar cells, water splitting devices, photocatalysis and sensors.

Acknowledgements

This work was financially supported by the National Natural Science Foundation of China (No. 21131001), the Open Subject Foundation of Key Laboratory of Polyoxometalate Science of Ministry of Education (No. 130014553), the Science and Technology Research Foundation of the Thirteenth Five Years of Jilin Educational Committee, the Technology Foundation for Selected Overseas Chinese Scholars, Ministry of Personnel of China and the Analysis and Testing Foundation of Northeast Normal University.

Notes and references

1 L. Cronin and A. Müller, *Chem. Soc. Rev*., 2012, **41**, 7333.
2 N. S. Lewis, *Science*, 2016, **351**, 353.
3 D. Sengupta, P. Das, B. Mondal and K. Mukherjee, *Renew. Sustain. Energy. Rev.*, 2016, **60**, 356.
4 J. Liu, Y. Liu, N. Y. Liu, Y. Z. Han, X. Zhang, H. Huang, Y. Lifshitz, S. T. Lee, J. Zhong and Z. H. Kang, *Science*, 2015, **347**, 970.
5 X. Zhang, Y. Liu, S. T. Lee, S. Yang and Z. H. Kang, *Energy Environ. Sci.*, 2014, **7**, 1409.
6 T. L. Ye, J. H. Wang, G. H. Dong, Y. X. Jiang, C. Feng and Y. L. Yang, *Chin. J. Chem.*, 2016, DOI: 10.1002/cjoc.201600231.
7 J. Liu, S. Y. Zhao, C. X. Li, M. M. Yang, Y. M. Yang, Y. Liu, Y. Lifshitz, S. T. Lee and Z. H. Kang, *Adv. Energy. Mater.*, 2016, DOI: 10.1002/aenm.201502039.
8 P. C. Yin, P. F. Wu, Z. C. Xiao, D. Li, E. Bitterlich, J. Zhang, P. Cheng, D. V. Vezenov, T. B. Liu and Y. G. Wei, *Angew. Chem. Int. Ed.*, 2011, **123**, 2569.
9 G. F. Cai, M. Q. Cui, V. P. Kumar, P. Darmawan, J. X. Wang, X. Wang, A. L. Eh, K. Qian and P. S. Lee, *Chem. Sci.*, 2016, **7**, 1373.
10 X. Wang, S. N. Zhao, Y. B. Zhang, Z. Wang, J. Feng, S. Y. Song and H. J. Zhang, *Chem. Sci.*, 2016, **7**, 1109.
11 F. D. Angelis, S. Fantacci, A. Selloni, M. K. Nazeeruddin and M. Grätzel, *J. Am. Chem. Soc.*, 2007, **129**, 14156.
12 L. A. Cameron, J. W. Ziller and A. F. Heyduk, *Chem. Sci.*, 2016, **7**, 1807.
13 M. Vasilopoulou, E. Polydorou, A. M. Douvas, L. C. Palilis, S. Kennouc and P. Argitis, *Energy Environ. Sci.*, 2015, **8**, 2448.
14 H. N. Hieu, N. Q. Dung, J. Kim and D. Kim, *Nanoscale*, 2013, **5**, 5530.
15 P. Roy, S. Berger and P. Schmuki, *Angew. Chem. Int. Ed.*, 2011, **50**, 2904.
16 A. Hagfeldt, G. Boschloo, L. C. Sun, L. Kloo and H. Pettersson, *Chem. Rev.*, 2010, **110**, 6595.
17 J. Tian, Z. H. Zhao, A. Kumar, R. I. Boughtonc and H. Liu, *Chem. Soc. Rev*., 2014, **43**, 6920.
18 F. K. Meng, J. T. Li, S. K. Cushing, M. J. Zhi and N. Q. Wu, *J. Am. Chem. Soc.*, 2013, **135**, 10286.
19 H. Y. Chen, Y. F. Xu, D. B. Kuang, C. Y. Su, *Energy Environ. Sci.*, 2014, **7**, 3887.
20 Z. X. Sun, Y. Z. Zhang, N. Li, L. Xu and T. Q. Wang. *J. Mater. Chem. C*, 2015, **3**, 6153.
21 L. Chen, W. L. Chen, H. Q. Tan, J. S. Li, X. J. Sang and E. B. Wang, *J. Mater. Chem. A*, 2016, **4**, 4125.
22 C. H. Shan, H. Zhang, W. L. Chen, Z. M. Su and E. B. Wang, *J. Mater. Chem. A*, 2016, **4**, 3297.
23 X. W. Guo, J. S. Li, X. J. Sang, W. L. Chen, Z. M. Su and E. B, Wang, *Chem. Eur. J.,* 2016, **22**, 3234.
24 S. S. Xu, W. L. Chen, Y. H. Wang, Y. G. Li, Z. J. Liu, C. H. Shan, Z. M. Su and E. B. Wang, *Dalton Trans.*, 2015, **44**, 18553.
25 X. J. Sang, J. S. Li, L. C. Zhang, Z. J. Wang, W. L. Chen, Z. M. Zhu, Z. M. Su and E. B. Wang, *ACS Appl. Mater. Interfaces.*, 2014, **6**, 7876.
26 G. Jin, S. M. Wang, W. L. Chen, C. Qin, Z. M. Su and E. Bo Wang, *J. Mater. Chem. A*, 2013, **1**, 6727.
27 J. S. Li, X. J. Sang, W. L. Chen, L. C. Zhang, Z. M. Zhu, Y. G. Li, Z. M. Su and E. B. Wang, *J. Mater. Chem. A*, 2015, **3**, 14573.
28 A. Müller, E. Krickemeyer, H. Bögge, M. Schmidtmann and F. Peters, *Angew. Chem. Int. Ed.*, 1998, **37**, 3359.
29 A. Rezaeifard, R. Haddad, M. Jafarpour and M. Hakimi, *J. Am. Chem. Soc.*, 2013, **135**, 10036.
30 I. Baroudi, C. S. Jegat, C. R. Marchal, N. L. Laronze, C. Livage, C. Martineau, C. Gervais, E. Cadot, F. Carn, B. Fayolle, and N. Steunou, *Chem. Mater.*, 2015, **27**, 1452.
31 T. Tachikawa, S. Tojo, M. Fujitsuka and T. Majima, *Chem. Eur. J.*, 2006, **12**, 3124.
32 X. Lopez, J. J. Carbo, C. Bo and J. M. Poblet, *Chem. Soc. Rev.*, 2012, **41**, 7537.
33 L. H. Sun, L. Y. Guo, J. S. Li, J. P. Bai, F. Su, L. C. Zhang, X. J. Sang, W. S. You and Z. M. Zhu, *ChemSusChem.*, 2016, **9**, 1125.
34 M. Vasilopoulou, A. M. Douvas, L. C. Palilis, S. Kennou and P. Argitis, *J. Am. Chem. Soc.*, 2015, **137**, 6844.
35 K. G. Lim, S. Ahn, Y. H. Kim, Y. B. Qi and T. W. Lee, *Energy Environ. Sci.*, 2016, **9**, 932.
36 C. Bo and P. Miró, *Dalton Trans.*, 2012, 41, 9984.
37 P. L. Kuo and C. H. Liao, *J. Power Sources*., 2015, **275**, 720.
38 Y. Z. Zhang, R. Tao, X. M. Zhao, Z. X. Sun, Y. J .Wang and L. Xu, *Chem. Commun.*, 2016, **52**, 3304.
39 K. Nagaveni, M. S. Hegde, N. Ravishankar, G. N. Subbanna and G. Madras, *Langmuir*, 2004, **20**, 2900.
40 J. L. G. Fierro, L. A. Arrua, J. M. N. Lopez and G. Kremenic, *Appl. Catal.*, 1988, **37**, 323.
41 Z. H. Kang, Y. Liu, C. H. A. Tsang, D. D. D. Ma, E. B. Wang and S. T. Lee, *Chem. Commun.*, 2009, 413.
42 P. Garrigue, M. H. Delville, C. Labruge`re, E. Cloutet, P. J. Kulesza, J. P. Morand and A. Kuhn, *Chem. Mater.*, 2004, **16**, 2984.
43 Y. Wei, L. T. Kong, R. Yang, L. Wang, J. H. Liu and X. J. Huang. *Chem. Commun.*, 2011, **47**, 5340.
44 E. P. Randviir and C. E. Banks. *Anal. Methods*, 2013, **5**, 1098.
45 F. Wang, Y. L. Zhang, Y. Liu, X. F. Wang, M. R. Shen, S. T. Lee and Z. H. Kang, *Nanoscale*, 2013, **5**, 1831.
46 Y. Xu and M. A. A. Schoonen, *Am. Mineral.*, 2000, **85**, 543.
47 J. F. Qian, P. Liu, Y. Xiao, Y. Jiang, Y. L. Cao, X. P. Ai and H. X. Yang, *Adv. Mater*., 2009, **21**, 3663.
48 F. Bella, S. Galliano, M. Falco, G. Viscardi, C. Barolo, M. Grätzel and C. Gerbaldi, *Chem. Sci.*, 2016, DOI: 10.1039/c6sc01145d.
49 Z. Q. Ji, G. Natu and Y. Y. Wu, *ACS Appl. Mater. Interfaces.*, 2013, **5**, 8641.
50 J. Bisquert, A. Zaban, M. Greenshtein and I. Mora-Seró, *J. Am. Chem. Soc.*, 2004, **126**, 13550.
51 Y. X. Jiang, Y. L. Yang, L. S. Qiang, R. Q. Fan, H. P. Ning, L. Li, T. L. Ye, B. Yang, W. W. Cao, *J. Power Sources.*, 2015, **278**, 527.
52 S. Ito, P. Chen, P. Comte, M. K. Nazeeruddin, P. Liska, P. Pe´chy and M. Grätzel, *Res. Appl.*, 2007, **15**, 603.

Figure Abstract

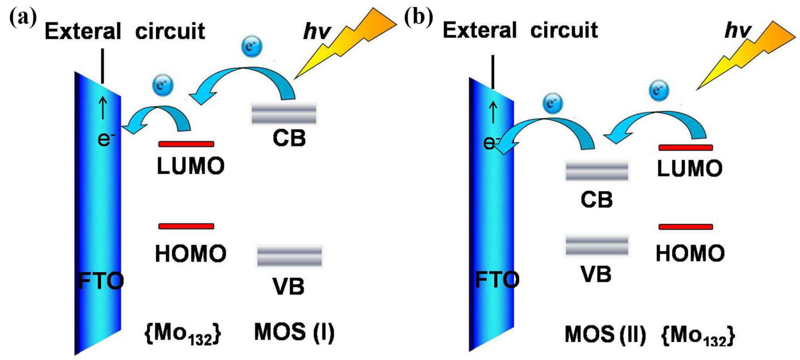

We designed and fabricated of POM/MOS composite photoelectrodes with light-enhanced conductivity. $\{Mo_{132}\}$ clusters act as photo-induced electron acceptor/donor to accelerate electron transfer and then improve their conductivity efficiently. Then the 5%$\{Mo_{132}\}/TiO_2$ composite photoelectrodes as photoanode in DSSCs exhibit the long electron lifetime (5.12 ms) and high PCE efficiency up to 7.94%, enhanced by 31% compared with pure TiO_2 (PCE, 6.06%) photoelectrodes.